Journal of Materials Chemistry C

ROYAL SOCIETY OF CHEMISTRY

PAPER

View Article Online
View Journal | View Issue

Check for updates

Cite this: J. Mater. Chem. C, 2024, 12, 8861

Unexpected p-type thermoelectric transport arising from magnetic Mn substitution in $Fe_2V_{1-x}Mn_xAl$ Heusler compounds†

Rajveer Jha,[a] Naohito Tsujii,[a]* Fabian Garmroudi,[b] Sergii Khmelevskyi,[c] Ernst Bauer[b] and Takao Mori[ad]*

Received 27th February 2024,
Accepted 22nd May 2024

DOI: 10.1039/d4tc00779d

rsc.li/materials-c

p-Type Fe_2VAl-based thermoelectrics have been much less investigated compared to their respective n-type counterparts. Thus, it is crucial to identify novel doping strategies to realize enhanced p-type Fe_2VAl Heusler compounds. In the current study, the effect of Mn substitution in $Fe_2V_{1-x}Mn_xAl$ is investigated with respect to temperature-dependent electronic transport as well as temperature- and field-dependent magnetic properties. We find an anomalous and unexpected p-type Seebeck coefficient for nominally n-doped $Fe_2V_{1-x}Mn_xAl$ over an extremely large range of concentrations up to x = 0.6. Using density functional theory (DFT) calculations, this is traced back to distinct modifications of the electronic structure, *i.e.*, localized magnetic defect states (m = 2.43μ_B) at the valence and conduction band edges, and a concomitant pinning of the Fermi level within the pseudogap. Furthermore, we were able to further optimize the thermoelectric properties by co-doping Al antisites in off-stoichiometric $Fe_2V_{0.9}Mn_{0.1}Al_{1+y}$, yielding sizeable values of the power factor, PF = 2.2 mW K^{-2} m^{-1} in $Fe_2V_{0.9}Mn_{0.1}Al_{1.1}$ at 350 K, and figure of merit, ZT ∼ 0.1 for highly off-stoichiometric $Fe_2V_{0.9}Mn_{0.1}Al_{1.5}$ at T = 500 K. Our work underlines the prospect of engineering Fe_2VAl-based Heusler compounds *via* magnetic doping to realize enhanced p-type thermoelectris and encourages studies involving other types of co-substitution for Mn-substituted $Fe_2V_{1-x}Mn_xAl$.

Introduction

Thermoelectric (TE) materials can convert waste heat into electric energy, or *vice versa*, by utilizing the Seebeck effect, thus representing a viable option for generating eco-friendly energy to address the current energy crisis.[1–4] A crucial task, however, lies in further improving the conversion efficiency of thermoelectric materials.[5,6] The efficiency of TE materials is determined by a dimensionless figure of merit $(ZT) = (S^2/\rho\kappa) \times T$, where S is the Seebeck coefficient, ρ the electrical resistivity, $\kappa = (\kappa_{elec} + \kappa_{ph})$ the thermal conductivity, consisting of electron and lattice contributions, and T the temperature. These key properties have tradeoffs that limit progress in enhancing ZT, and it is necessary to develop new enhancement principles.[7–9]

Among several material classes, the Heusler-type intermetallic compound Fe_2VAl is a promising candidate for thermoelectric power generation near room temperature.[10,11] This alloy has the cubic $L2_1$-ordered crystal structure and exhibits a high thermoelectric power factor PF = S^2/ρ near room temperature.[12] Fe_2VAl shows a semiconductor-like temperature dependence of the electrical resistivity in a wide temperature range up to 1200 K or above.[10] The electronic structure of stoichiometric Fe_2VAl suggests a deep pseudogap at the Fermi level.[13] Stoichiometric Fe_2VAl is a nonmagnetic, low carrier, and compensated semimetal.[13–18] Recently, it was shown that rational co-substitution can tune the band gap and therefore significantly improve the thermoelectric properties, yielding high power factors up to around 10.3 mW K^{-2} m^{-1}.[19–22] However, the lattice thermal conductivity of Fe_2VAl is about one order of magnitude larger than that of other high-performance thermoelectric materials, resulting in much smaller ZT values compared to the best-performing systems at room temperature like Bi_2Te_3 or Mg_3Sb_2-based compounds.[6,23–28]

In order to further increase ZT of Fe_2VAl-based systems, various strategies have been employed already, including elemental substitution at all lattice sites, tuning the microstructure and grain size as well as thin film deposition.[29–50] Particularly, B. Hinterleitner *et al.* reported an ultrahigh power

[a] Research Center for Materials Nanoarchitectonics (MANA), Nanomaterials Field, National Institute for Materials Science (NIMS), 1-2-1 Sengen, Tsukuba 305-0047, Japan. E-mail: tsujii.naohito@nims.go.jp, mori.takao@nims.go.jp
[b] Institute of Solid State Physics, TU Wien, A-1040 Vienna, Austria
[c] Vienna Scientific Cluster Research Center, TU Wien, A-1040 Vienna, Austria
[d] Graduate School of Pure and Applied Sciences, University of Tsukuba, Tennodai 1-1-1, Tsukuba 305-8671, Japan

† Electronic supplementary information (ESI) available. See DOI: https://doi.org/10.1039/d4tc00779d

factor, above 45 mW K^{-2} m^{-1}, and ZT around 5 at 350 K for $Fe_2V_{0.8}W_{0.2}Al$ metastable thin films.[50] Also, doping of Fe_2VAl p-type Heusler compounds with various elements, such as Ti and Zr, has been studied to understand the effects of different dopants on the thermoelectric performance.[40,51,52] However, the performance of p-type Fe_2VAl-based thermoelectrics remains still far below those of the best n-type compounds. Therefore, it is crucial to identify novel p-type candidate materials and doping elements.

Furthermore, it has been demonstrated that spin fluctuations can contribute significantly to optimize the power factor (PF = 1.2 mW K^{-2} m^{-1} at 400 K) in weakly ferromagnetic $Fe_2V_{0.9}Cr_{0.1}Al_{0.9}Si_{0.1}$ and $Fe_{2.2}V_{0.8}Al_{0.6}Si_{0.4}$.[53] That being said, likewise to spin fluctuations, the usage of magnetism in different forms to enhance the Seebeck coefficient is also rapidly increasing; for example, spin Seebeck effect, anomalous Nernst effect, magnon drag, paramagnon drag, spin entropy, *etc.*[54–61] are most recently studied instances.

Thus, magnetic doping can be a useful strategy in improving thermoelectric properties. In the case of Fe_2VAl-based compounds, however, the effect of magnetic element doping with respect to thermoelectric properties, has not been well studied. This motivated us to substitute V/Mn in $Fe_2V_{1-x}Mn_xAl$. We observed a unusual hole-dominated Seebeck coefficient in nominally n-doped $Fe_2V_{1-x}Mn_xAl$, which increases with increasing Mn content up to $x = 0.2$. Employing first principles electronic structure calculations within the framework of the density functional theory[62] and the coherent potential approximation,[63] used to model the effects of the substitutional atomic disorder, we trace this back to a severe modification of the electronic structure, wherein magnetic impurity states are formed by Mn atoms, leading to a pinning of the Fermi energy near the valence band edge and within the pseudogap.

Moreover, we additionally co-substituted Al antisites at the Fe and V sites in Al-rich $Fe_2V_{0.9}Mn_{0.1}Al_{1+y}$ samples to further optimize the thermoelectric performance. Since p-type Fe_2VAl Heusler compounds have been reported to a lesser content compared to n-type systems, we systematically studied the effect of combined Al off-stoichiometry and Mn co-substitution in p-type $Fe_2V_{1-x}Mn_xAl_{1+y}$. As an extra finding, the thermal conductivity is substantially suppressed already in single-substituted $Fe_2V_{1-x}Mn_xAl$ and even further by introducing additional Al off-stoichiometry in $Fe_2V_{1-x}Mn_xAl_{1+y}$. Moreover, the latter shows a sizeable enhancement of the thermopower and a shift of the maximum towards higher temperatures, together with an unexpectedly low electrical resistivity. It is crucial to focus on and optimize p-type full-Heusler systems suitable for applications in thermoelectric power generation, because the well-studied n-type material must be paired with a p-type counterpart to assemble efficient thermoelectric modules.

Experimental & computational details

High-purity elements of Fe (99.98%), Mn (99.99%), V (99.9%), and Al (99.999%), were weighted in the stoichiometric ratio and were arc-melted in Ar atmosphere on a water-cooled copper hearth. The ingots were turned over on the copper hearth and were re-melted for four times to ensure homogeneity. The obtained ingots were loaded to a tungsten carbide jar in the glove box under an Ar atmosphere and milled to a fine powder in a planetary ball mill at a speed of 200 rpm for 5 hours. The obtained fine powders were loaded in a graphite die and consolidated by spark plasma sintering (SPS, SPS-1080 System, SPS SYNTEX INC) under a pressure of 40 MPa at 1273 K for 10 minutes under static vacuum (2×10^{-2} Pa). We performed post-annealing for all the samples after the SPS sintering the samples were sealed in quartz tubes for high-temperature annealing at 1273 K for 24 hours and then slowly cooled down to 673 K in 48 hours, where the samples were further annealed for 48 hours and finally naturally cooled to room temperature.

Powder X-ray diffraction measurements were performed to check the phase purity and lattice parameters of the cubic Heusler compounds using a RINT TTR-3 diffractometer (Rigaku Co., Akishima, Tokyo, Japan) and employing Cu K_α radiation. Experimental data were further analyzed by the Rietveld refinement method using the program RIETAN-FP.[64] Finally, bar-shaped samples were cut out of the disk samples and used to measure the Seebeck coefficient and electrical resistivity. Measurements were done with a four-probe method on a commercial system ZEM3 (Advance Riko Inc.). The thermal conductivity κ was calculated by using $\kappa = DC_pd$, where D is the thermal diffusivity, C_p is heat capacity, and d is density. The thermal diffusivity coefficient (D) and the heat capacity (C_p) of bulk material were concurrently measured for the disk sample on a xenon laser flash system (Netzsch LFA 467, Germany) with a pyro Ceram disk as a reference sample. Magnetization measurements were performed by using a superconducting quantum interference device magnetometer from Quantum Design.

Density functional theory calculations of the electronic structure of $Fe_2V_{1-x}Mn_xAl$ were performed using the coherent potential approximation (CPA) in the framework of the Korringa–Kohn–Rostoker (KKR) method and the atomic sphere approximation (ASA).[65,66] In our KKR–ASA calculations the partial wave functions were expanded in a spdf-basis (up to $l = 3$) and the effects of exchange and correlation are treated within the density functional theory using standard PBE exchange–correlation functionals.[62] To model thermal magnetic disorder above the magnetic ordering temperature, we employed the disordered local moments (DLM) formalism.[67]

Results and discussion

Fig. 1(a) and (c) shows the powder X-ray diffraction patterns for $Fe_2V_{1-x}Mn_xAl$ and $Fe_2V_{0.9}Mn_{0.1}Al_{1+y}$ samples, respectively. All the samples crystallize in the Heusler ($L2_1$) type structure; no impurity peak or secondary phase has been observed. The (111) peak at around 27° is not very pronounced and is further suppressed with increasing Mn or Al concentration in $Fe_2V_{1-x}Mn_xAl$ or $Fe_2V_{0.9}Mn_{0.1}Al_{1+y}$ [see Fig. S1(a) and (b) in the ESI†]. The suppressing of the (111) peak suggests that disorder in the

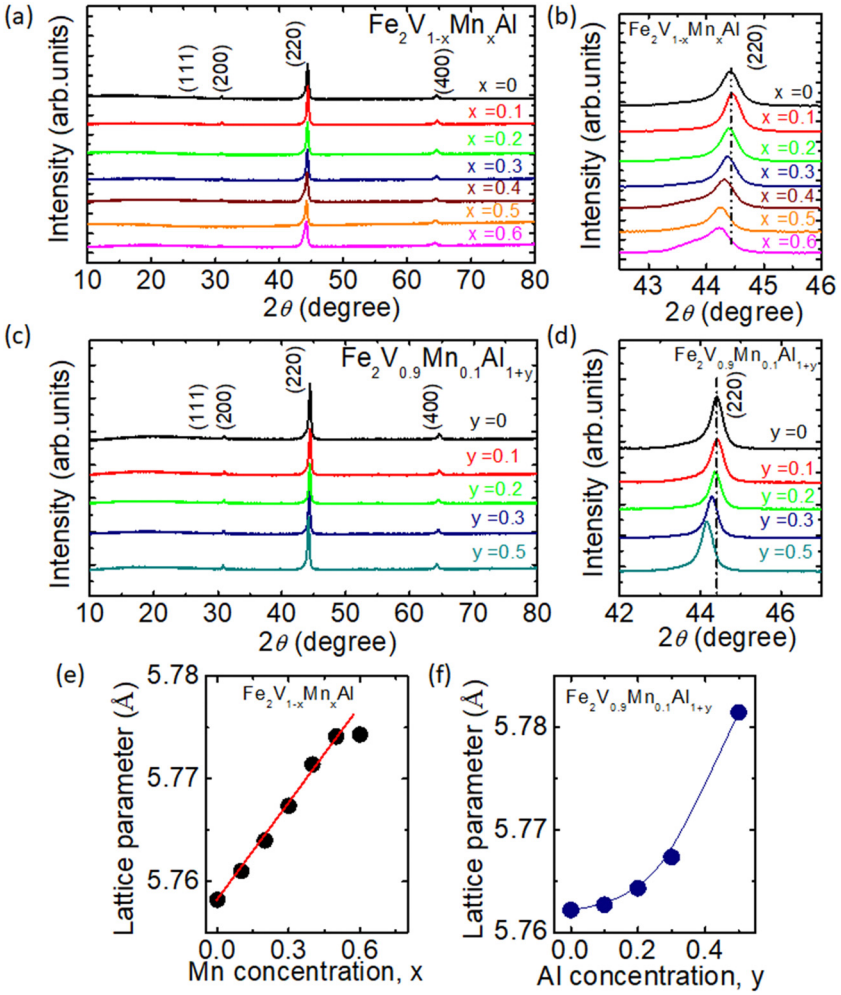

Fig. 1 (a) XRD patterns for $Fe_2V_{1-x}Mn_xAl$ sintered samples, with the numbers in the XRD pattern indicating Miller indices. (b) Zoomed view of (220) peak at around 44.5° for $Fe_2V_{1-x}Mn_xAl$. (c) XRD patterns for $Fe_2V_{0.9}Mn_{0.1}Al_{1+y}$ sintered samples. (d) Zoomed view of (220) peak at around 44.5° for $Fe_2V_{0.9}Mn_{0.1}Al_{1+y}$. (e) The lattice parameter was obtained by a refinement using the Rietveld method with RIETAN-FP[64] of $Fe_2V_{1-x}Mn_xAl$ as a function of concentration x of Mn, and the solid line represents the linear Vegard's law. (f) Lattice parameter obtained by a refinement of $Fe_2V_{0.9}Mn_{0.1}Al_{1+y}$ as a function of y.

Fe_2VAl compound becomes more significant with doping. Because the 111 peak is mainly due to the difference in the scattering factors of the Al and the V-sites, our findings indicate that an inter-atomic B2-type disorder exists between the two sites. The (220) peak at around 44.5° for $Fe_2V_{1-x}Mn_xAl$ and $Fe_2V_{0.9}Mn_{0.1}Al_{1+y}$ is shown in Fig. 1(b) and (d), indicating a steady increase in the lattice parameter with increasing Mn/Al concentration. The broadening of (220) peak with increasing Mn concentration indicates that disorder is increasing in Mn-doped Fe_2VAl compounds. Also, the grain size reduction is another possibility of broadening of (220) peak. Moreover, the lattice parameter was obtained by Rietveld analysis for all samples. Fig. 1(e) and (f) exhibits the lattice parameters as a function of the concentration x and y for the Mn-doped and Al-rich samples, respectively. The increase in the lattice parameter with Mn doping is basically in line with Vegard's law. Also, we observed a slight deviation from Vegard's law for high Mn concentration, *i.e.*, $x = 0.6$.[68] Furthermore, we found that the lattice parameter for Al-rich $Fe_2V_{0.9}Mn_{0.1}Al_{1+y}$ is increasing with increasing Al doping. The increase of the lattice parameter with y in $Fe_2V_{0.9}Mn_{0.1}Al_{1+y}$ does not follow Vegard's law. Moreover, the lattice parameter increases rapidly for $y = 0.5$, which deviates from previously reported results for the Al-rich Fe_2VAl_x.[69] Nonetheless, the overall tendency of an increasing lattice parameter is consistent with that reported on Al-rich Fe_2VAl_x, although the absolute values are smaller compared to those reported previously. The linear trend observed in the lattice parameter indicates that Mn atoms successfully substitute the V site; the solubility limit of Al in Al-rich $Fe_2V_{0.9}Mn_{0.1}Al_{1+y}$ is $y = 0.5$. In comparison, the solubility limit of Al in pure Fe_2VAl_x was found to be $x = 2$ in ref. 64. For Al-rich $Fe_2V_{0.9}Mn_{0.1}Al_{1+y}$, the off-stoichiometry manifests itself through the presence of Al antisites on the Fe and V sites.[69] Overall, the crystallographic site occupancies can considerably affect the physical properties of Heusler compounds.[70]

Fig. 2 depicts the temperature-dependent thermoelectric properties of $Fe_2V_{1-x}Mn_xAl$. Firstly, the electrical resistivity at T = 300 K shows a slight increase as x increases up to x = 0.1, then gradually decreases with further increasing the Mn concentration in $Fe_2V_{1-x}Mn_xAl$ [Fig. 2(a)]. We note that the Seebeck coefficient for stoichiometric Fe_2VAl (x = 0) is slightly negative in this study, whereas usually sizeable positive values have been reported for samples synthesized *via* arc or induction melting.[45,71] This discrepancy can likely be explained by off-stoichiometry or antisite disorder induced during the synthesis *via* ball milling and has been found by other groups as well.[72,73] However, the Seebeck coefficient becomes p-type upon substituting Mn at the V site in $Fe_2V_{1-x}Mn_xAl$, even though n-type doping would be expected from a simple estimation of the effective valence electron concentration per atom, indicating non-rigid band doping behavior. The absolute value of the Seebeck coefficient reaches S = 64 μV K^{-1} at 300 K for $Fe_2V_{1-x}Mn_xAl$ with x = 0.2 [Fig. 2(b)]. For higher Mn-doped samples, the Seebeck coefficient decreases down to S = 16 μV K^{-1} at 300 K for $Fe_2V_{1-x}Mn_xAl$ (x = 0.6). For non-doped Fe_2VAl, the Seebeck coefficient is almost temperature-independent, and the absolute value is near to zero. Again, these results deviate significantly from those obtained in melted samples and suggest the presence of defects such as antisites in the present sample. The highest value of the power factor PF = 0.8 mW K^{-2} m^{-1} [Fig. 2(c)] is obtained for $Fe_2V_{0.8}Mn_{0.2}Al$ and peaks near room temperature, like all the other samples from $Fe_2V_{1-x}Mn_xAl$.

The total thermal conductivity of $Fe_2V_{1-x}Mn_xAl$ [Fig. 2(d)], κ, is nearly temperature-independent, and the values decrease substantially upon Mn doping in $Fe_2V_{1-x}Mn_xAl$. The total thermal conductivity at room temperature for stoichiometric Fe_2VAl is 16 W m^{-1} K^{-1}, which is significantly lower than for melted samples (~25–30 W m^{-1} K^{-1}),[74,75] again indicating an increased number of defects such as antisite disorder, lattice strain, and grain boundaries that likely arise from the synthesis *via* ball milling. For $Fe_2V_{1-x}Mn_xAl$ (x = 0.6), the thermal conductivity further decreases down to 9 W m^{-1} K^{-1}. In general, the total thermal conductivity κ for ordinary metals and semimetals is the sum of electronic and phonon terms, which can be specified as $\kappa = \kappa_{elec} + \kappa_{ph}$, where κ_{ph} is the lattice thermal conductivity and κ_{elec} is the electronic contribution, although a bipolar share should be expected when minority carriers actively contribute to transport. Since previous studies on Fe_2VAl-based systems have neglected the bipolar contribution, we align our investigation with those works and only distinguish between lattice and electron contributions, where κ_{el} is related to the electrical resistivity ρ as given by the Wiedemann–Franz law $\kappa_{el} = L_0T/\rho$, where L_0 = 2.45 × 10^{-8} WΩ K^{-2} is the Lorenz number, and ρ is the electrical resistivity. The lattice thermal conductivity (κ_{ph}) can be obtained by subtracting κ_{el} from the total thermal conductivity (κ). Fig. 3(a) shows κ_{ph} as a function of temperature. At room temperature, κ_{ph} drops from 14 to 7.5 W m^{-1} K^{-1} due to the Mn substitution, which is a significant reduction compared to previously reported values for doped Fe_2VAl systems,[12,30,74,76–78] considering that there are no significant differences in atomic mass and size between Mn and V atoms. Meanwhile, it is obvious that κ_{elec} is smaller than κ_{ph} for all the studied compounds, which signifies that the total thermal conductivity is dominated by lattice phonons rather than charge carriers. This implies that a substantial further enhancement can be achieved by further suppressing

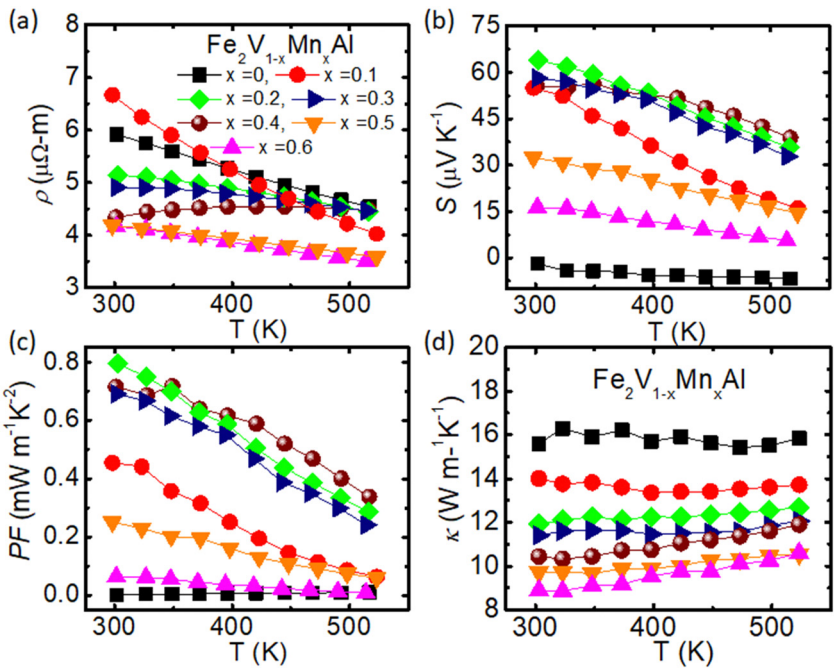

Fig. 2 Thermoelectric properties of $Fe_2V_{1-x}Mn_xAl$ (x = 0, 0.1, 0.2, 0.3, 0.4, 0.5 and 0.6) (a)–(d) temperature dependence of electrical resistivity ρ, Seebeck coefficient S, power factor PF, and total thermal conductivity κ, respectively.

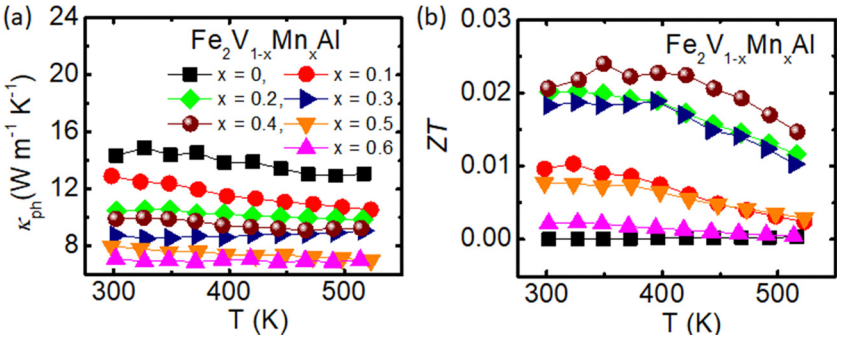

Fig. 3 (a) Temperature dependence of lattice thermoelectric conductivity for $Fe_2V_{1-x}Mn_xAl$. (b) The thermoelectric performance, *ZT* values *vs.* temperature for $Fe_2V_{1-x}Mn_xAl$.

heat conduction through phonons, *e.g.* by tuning the microstructure or *via* co-substitution as employed in the second part of this study. The dimensionless figure of merit, *ZT*, was determined and reaches its highest value $ZT = 0.025$, for $Fe_2V_{1-x}Mn_xAl$ ($x = 0.4$) at about $T = 350$ K [Fig. 3(b)].

In order to further improve the TE properties of Mn-substituted $Fe_2V_{1-x}Mn_xAl$, additional co-substitution/off-stoichiometry with Al at the Fe and V sites has been performed. This type of off-stoichiometry has been previously shown to not only significantly increase the p-type Seebeck coefficient of Fe_2VAl-based thermoelectrics but also greatly reduces the lattice thermal conductivity *via* substitutions on different sublattices.[69] Fig. 5 demonstrates the temperature-dependent thermoelectric properties of Al-rich $Fe_2V_{0.9}Mn_{0.1}Al_{1+y}$. Indeed, within this study we have observed that ρ decreases with increasing Al concentration (see Fig. 5(a)). Furthermore, the temperature-dependent behavior of $\rho(T)$ changes from semiconductor-like, $d\rho/dT < 0$, towards metallic-like, $d\rho/dT > 0$. It is interesting to note, however, that ρ reaches its lowest values for $Fe_2V_{0.9}Mn_{0.1}Al_{1.3}$ ($y = 0.3$) and increases again dramatically as y further rises up to $y = 0.5$, concomitant with an unexpected decrease of the carrier concentration. This indicates peculiar changes in the electronic structure and clearly shows that such Al off-stoichiometry cannot be regarded as a conventional doping mechanism.

Regarding the Seebeck coefficient, the additional off-stoichiometry clearly has a beneficial effect and not only increases the absolute values of the Seebeck coefficient but also modifies the overall temperature-dependent behavior such that S stays large over a broader temperature interval (see Fig. 5(b)). Upon increasing the amount of Al in $Fe_2V_{0.9}Mn_{0.1}Al_{1+y}$, the maximum of $|S|$ shifts from below room temperature up to almost 500 K for $Fe_2V_{0.9}Mn_{0.1}Al_{1.5}$ ($y = 0.5$). Moreover, the peak value $S = 82$ μV K^{-1} for $Fe_2V_{0.9}Mn_{0.1}Al_{1.5}$ ($y = 0.5$) is about 20% larger than the maximum value of the $Fe_2V_{1-x}Mn_xAl$ series, $S = 61$ μV K^{-1} for $x = 0.2$ (shown in Fig. 3(b)). Hence, as expected, the Al-excess in terms of antisites on Fe and V sublattices has brought an enhancement in the Seebeck coefficient, consistent with findings in ref. 69. The value $S = 82$ μV K^{-1} is comparable to the largest ones in the p-type Fe_2VAl-based systems[12,19,44–49,69,74] and establishes such type of Al-off stoichiometry and concomitant co-substitution, *e.g.*, with V/Mn, as a desirable route to improve the *ZT* of p-type full-Heusler systems. The temperature dependence of the Seebeck coefficient shows a maximum at around $T = 350$ K for $y = 0.1$ and 0.2, and around $T = 450$ K for $x = 0.3$ and 0.5. The maximum for $y = 0$ is not seen in Fig. 4(b), but is expected below $T = 300$ K. Thus, the maximum temperature systematically increases with increasing y. This reflects the increase in the hole carrier concentration by extra Al doping and also hints at a possible expansion of the band gap.

Compared to the single substitution series $Fe_2V_{1-x}Mn_xAl$, where the power factor peaks at 0.8 mW K^{-2} m^{-1}, PF is significantly improved up to 2.0 mW K^{-2} m^{-1} for $Fe_2V_{0.9}Mn_{0.1}Al_{1.1}$. However, the power factor decreases with increasing Al concentration in $Fe_2V_{0.9}Mn_{0.1}Al_{1+y}$, hovering around PF = 1.6–1.8 mW K^{-2} m^{-1} at 450–500 K for $y = 0.3$ and 0.5. The thermal conductivity of $Fe_2V_{0.9}Mn_{0.1}Al_{1+y}$ shows only weak temperature dependence for the measured temperature range 300–550 K (see Fig. 5(d)). The thermal conductivity at room temperature for stoichiometric $Fe_2V_{0.9}Mn_{0.1}Al$, is 12.1 W m^{-1} K^{-1}, while it decreases monotonically as a function of y down to 9 W m^{-1} K^{-1} for $Fe_2V_{0.9}Mn_{0.1}Al_{1+y}$ ($y = 0.5$). We observed an almost 40% drop in thermal conductivity for $Fe_2V_{0.9}Mn_{0.1}Al_{1+y}$ ($y = 0.5$) compared to the stoichiometric Fe_2VAl compound, despite the lack of any heavy element substitution in the investigated samples. The significant decreases in thermal conductivity with increasing Al in $Fe_2V_{0.9}Mn_{0.1}Al_{1+y}$ is consistent with the findings in ref. 69 and is assumed to be stemming from the sizeable atomic disorder and point defects brought about by the large number of Al/Fe and Al/V antisites.

The temperature dependence of κ_{ph} is shown in Fig. 5(a), which was again obtained by applying the Wiedemann–Franz law to estimate the electronic contribution from the experimental electrical resistivity. Overall, the thermal conductivity is phonon-driven, while the κ_{elec} contribution increases for Al-rich samples. As discussed in the previous section, the electrical resistivity was further decreased, and the Seebeck coefficient enhanced for the Al-rich $Fe_2V_{0.9}Mn_{0.1}Al_{1+y}$ samples, Consequently, the power factor has improved, and thermal conductivity decreased for Al-rich $Fe_2V_{0.9}Mn_{0.1}Al_{1+y}$ samples. Moderately, the *ZT* values have been improved for $Fe_2V_{0.9}Mn_{0.1}Al_{1+y}$ ($y = 0.5$), with the

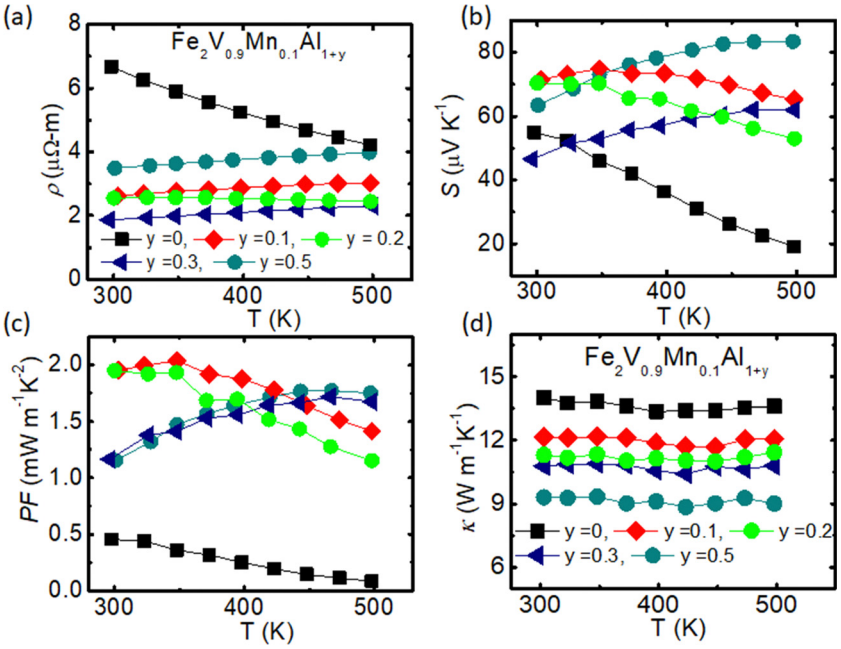

Fig. 4 Thermoelectric properties of $Fe_2V_{0.9}Mn_{0.1}Al_{1+y}$ (y = 0, 0.1, 0.2, 0.3 and 0.5) (a)–(d) temperature dependence of electrical resistivity ρ, Seebeck coefficient S, power factor PF, and total thermal conductivity κ, respectively.

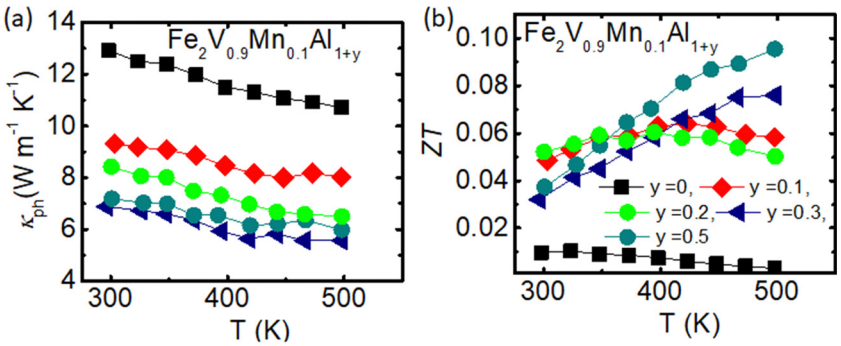

Fig. 5 (a) Temperature dependence of lattice thermoelectric conductivity for $Fe_2V_{0.9}Mn_{0.1}Al_{1+y}$. (b) The thermoelectric performance, ZT values *vs.* temperature for $Fe_2V_{0.9}Mn_{0.1}Al_{1+y}$.

highest ZT value 0.1 achieved for $Fe_2V_{0.9}Mn_{0.1}Al_{1+y}$ (y = 0.5) at around T = 500 K [Fig. 5(b)].

Furthermore, we have investigated the valence electron concentration (VEC) dependence of the Seebeck coefficient (S) at T = 300 K for $Fe_2V_{1-x}Mn_xAl$ and $Fe_2V_{0.9}Mn_{0.1}Al_{1+y}$. Fe_2VAl has 24 valence electrons per formula unit, thereby VEC = 6.[40] As aliovalent elements are doped in the Fe_2VAl system, the VEC deviates from 6, which affects largely the Seebeck coefficient. For Mn-doped $Fe_2V_{1-x}Mn_xAl$, the VEC scenario is not in agreement with the behavior observed within the majority of single-element doping studies reported in the literature so far; rather, we have observed a p-type Seebeck coefficient for the VEC > 6.0 (see Fig. 7(a)). The universal curve based on the VEC is only valid for the rigid band case.[40] However, substitutions on the Fe- or V-sites with certain transition metals, can cause significant changes in the electronic band structure; thereby, the simple VEC rule is no longer valid. For instance, off-stoichiometric Heusler alloys, $Fe_{2-x}V_{1+x-y}Ti_yAl$ (p-type Seebeck coefficient), have been investigated using soft X-ray photoelectron spectroscopy.[79] The electronic structure near the Fermi level is found to be drastically altered by off-stoichiometry, while doping with Ti has a more moderate effect in a rigid-band-like manner.[79] In the case of off-stoichiometric $Fe_{2-x}V_{1+x}$ Al-based Heusler alloys, Soda *et al.* proposed that the excess V or Fe (antisite) defects may induce impurity states near the valence band edge, resulting in a potential enhancement of the Seebeck coefficient.[80] To elucidate the anomalous p-type Seebeck coefficient in nominally n-doped $Fe_2V_{1-x}Mn_xAl$, we have performed extensive density functional theory calculations of the alloy-averaged densities of states of substituted $Fe_2V_{1-x}Mn_xAl$, which are summarized in the subsequent section. Our theoretical investigations reveal that the Fermi level remains pinned near the valence band edge inside the pseudogap, owing to the creation of additional electronic states below E_F, which balances the chemical potential.

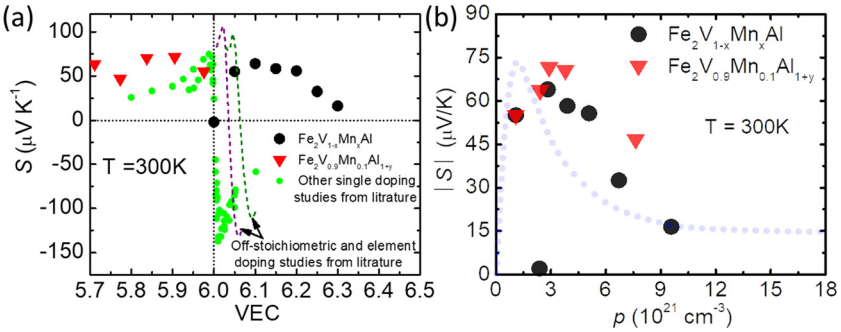

Fig. 6 (a) The Seebeck coefficient as a function of valence electron concentration (VEC) at 300 K. The dotted lines are doped off-stoichiometric Fe_2VAl data taken from ref. 78. (b) The Seebeck coefficient as a function of hole carrier concentration p estimated at T = 300 K for $Fe_2V_{1-x}Mn_xAl$ and $Fe_2V_{0.9}Mn_{0.1}Al_{1+y}$ with Ioffe–Pisarenko cure.

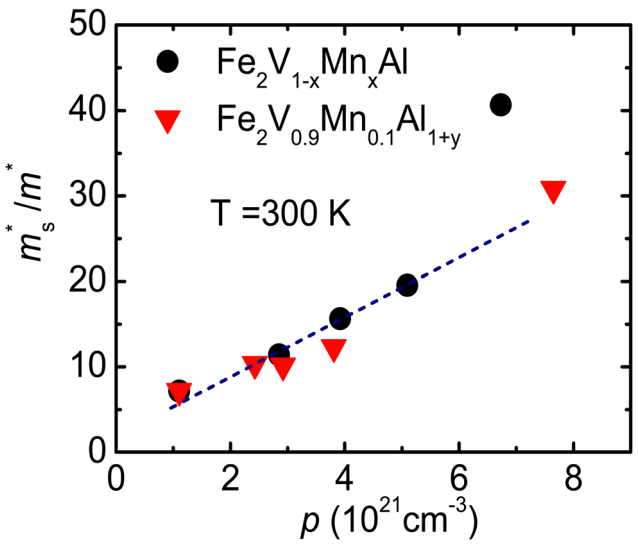

Fig. 7 The Seebeck effective mass (m_s^*) as a function of hole carrier concentration p estimated at T = 300 K for $Fe_2V_{1-x}Mn_xAl$ and $Fe_2V_{0.9}Mn_{0.1}Al_{1+y}$. The dotted line represents a linear trend in m_s^* with increasing Mn doping in $Fe_2V_{1-x}Mn_xAl$.

To further shed light on the anomalous doping dependence of $Fe_2V_{1-x}Mn_xAl$ and $Fe_2V_{0.9}Mn_{0.1}Al_{1+y}$, we have measured the Hall resistivity to estimate the carrier concentration.

The magnetic field-dependent Hall resistivity for $Fe_2V_{1-x}Mn_xAl$ and $Fe_2V_{0.9}Mn_{0.1}Al_{1+y}$ at T = 300 K is shown in the ESI† [see Fig. S7]. A linear magnetic field dependence ρ_{xy} was observed for all samples. The Hall coefficient R_H was then determined from the slope of ρ_{xy} *versus* the applied magnetic field B. The carrier concentration (p) was estimated using the simple equation $p = 1/eR_H$. All the samples (except for $x = 0$ and $y = 0$) are p-type, and the hole carrier concentration appears to increase monotonically with doping, except for $y = 0.5$.

The Seebeck coefficient as a function of carrier concentration at room temperature, known as the Ioffe–Pisarenko plot, is shown in Fig. 7(b). The results here deviate from the Ioffe–Pisarenko curve, especially in the heavily doped region. Although a general trend with a maximum is similar, a clear difference is that the peak is much wider than the normal IP curve, with a shift of maximum to higher carrier concentrations. This is consistent with an increase of the density of states effective mass. Indeed, DFT calculations reveal that rather localized electronic states are formed at both sides of the Fermi level and that the slope of the energy-dependent density of states is enhanced, which is in good agreement with experimental findings. Similar features were reported by Parzer *et al.* for the Al-rich Fe_2VAl system, where they suggested that a shift in a maximum of S *vs.* carrier concentration occurs due to resonant states located close to the Fermi level.[69] Therefore, Mn- and extra Al-doping can be a very fast and effective way to increase the Seebeck coefficient through disorder-related resonant levels in the Heusler compounds. In the present case, the Mn- and Al-doping provoked too much hole carriers, thereby the enhancement in the Seebeck coefficient was just moderate. It should also be stressed that thermally quenched samples of Fe_2VAl showed only n-type behavior and an effective strategy for enhancing the p-type Heusler compound has not been reported. The present findings, Mn- and/or excess Al-doping induced disorder may cast a new way for achieving p-type high power factor.

The Hall mobility was derived using $\mu_H = \rho_{xy}/(\rho_{xx}B)$ [see Table S2, ESI†]. μ_H decreases by increasing the Mn doping concentration in $Fe_2V_{1-x}Mn_xAl$ or increasing Al in $Fe_2V_{0.9}Mn_{0.1}Al_{1+y}$ due to the increasing charge carrier density and/or increasing static disorder in the crystalline unit cell.

Fig. 7 shows the Seebeck effective mass (m_s^*) as a function of hole carrier concentration p estimated at T = 300 K for $Fe_2V_{1-x}Mn_xAl$ and $Fe_2V_{0.9}Mn_{0.1}Al_{1+y}$. m_s^* was estimated using eqn (S1) (ESI†), where the m_s^* values are directly proportional to the Seebeck coefficient and the carrier concentration (p).[81] The formula used was taken from ref. 81 where it is suggested that there are two classes of effective masses; one describes an inertial effective mass that is relevant to a specific electron, and the other one depends more on the density of the electron states (DOS), and is hence called a DOS mass, m_{DOS}^*. Further, m_{DOS}^* can be directly calculated from the Seebeck coefficient employing eqn (S2) (ESI†); thus, m_{DOS}^* can be considered as Seebeck effective mass (m_s^*). We found that with increasing carrier concentration, the Seebeck effective mass m_s^* increases linearly in the case of $Fe_2V_{1-x}Mn_xAl$, while for the

$Fe_2V_{0.9}Mn_{0.1}Al_{1+y}$, it slightly deviates from linearity. According to literature, the tendencies of the Seebeck effective mass m_s^* at room temperature and above upon doping are straightforwardly explained by changes in the band structure, *e.g.*, band convergence or changes in the dominant scattering mechanism. In fact, it has been mentioned for Al-rich Fe_2VAl_x systems that a local distortion of the electronic density of states arises for very large Al concentrations.[69] Again, the increase of m_s^* is fully consistent with first-principles calculations, revealing a modification of the alloy-averaged densities of states, where both conduction and valence band edges become more steep. Thus, the density of states effective mass increases due to the rather localized impurity states by Mn, which spawn at both sides of the Fermi energy.

As can be seen in Fig. 6(a), p-type full Heusler materials have a smaller absolute value of the Seebeck coefficient compared to n-type materials. Additionally, it's challenging to obtain p-type materials due to a more restricted number of doping elements. Mn doping Al-rich Fe_2VAl could lead to improved thermoelectric properties in p-type materials near room temperature. The achieved power factor around 2.2 mW K^{-2} m^{-1} at T = 350 K, involving a Mn-doped Al-rich Fe_2VAl strategy, is larger than Ta-doped or Al-rich Fe_2VAl systems, while it is lower than for off-stoichiometric and Ti-doped samples, reaching up to ~4 mW K^{-2} m^{-1}.[12,52] In the present cases, the highest ZT value of 0.05 was achieved for $Fe_2V_{0.9}Mn_{0.1}Al_{1+y}$ (y = 0.1, 0.2) near room temperature. The value of power factor for Mn-doped Al-rich $Fe_2V_{0.9}Mn_{0.1}Al_{1+y}$ (y = 0.1) around 2.2 mW K^{-2} m^{-1} is a relatively high value for p-type Heusler compound near room temperature. The explored compounds could be useful for applications in thermoelectric power generation.

The magnetic properties of selected samples were also investigated. Fig. 8(a) depicts the temperature-dependent magnetization M under an applied external magnetic field B = 1 T for the $Fe_2V_{1-x}Mn_xAl$ (x = 0, 0.1, 0.2, 0.4) samples in the temperature range 2–300 K. We fitted the inverse of the magnetic susceptibility H/M *vs.* temperature measured at B = 1 T for x = 0, 0.1, 0.2 and 0.4 in the paramagnetic region above 200 K employing the Curie–Weiss function, $H/M = (T - \theta)/C$, where C and θ are the Curie constant and Weiss temperature, respectively [see Fig. 8(b)]. From least squares fit, the obtained values of parameters C, and θ are summarized in Table 1. Because of the decreasing Curie constants upon an increasing Mn content, the overall susceptibility decreases. The value of θ can be seen as a measure of the inter-site magnetic interaction in the case of a molecular-field approximation. Thus, the samples with x = 0 and 0.1 are weakly ferromagnetic, with a Weiss temperature θ = 35 K and θ = 50 K, respectively, which can most likely be attributed to intrinsic antisite defects involving the Fe sublattices.

A further increase of x, however, causes a crossover of θ to negative values (x = 0.4: $\theta \sim -16$ K), indicating that the growing Mn content triggers eventually antiferromagnetic interactions. This is very much in line with our first-principles calculations of the exchange interactions between Mn atoms shown in the ESI† (Table S7).

The derivative of magnetization dM/dT *vs.* T shows a peak at around 16 K for undoped Fe_2VAl and 30 K for x = 0.1, which suggests a Curie temperature $T_C \sim 16$ K for x = 0 and $T_C \sim 30$ K for x = 0.1 [see ESI,† Fig. S6(a)]. The isothermal magnetization at T = 2 K decreases rapidly with increasing Mn concentration in $Fe_2V_{1-x}Mn_xAl$ for $x \geq 0.2$. This decrease in magnetization is

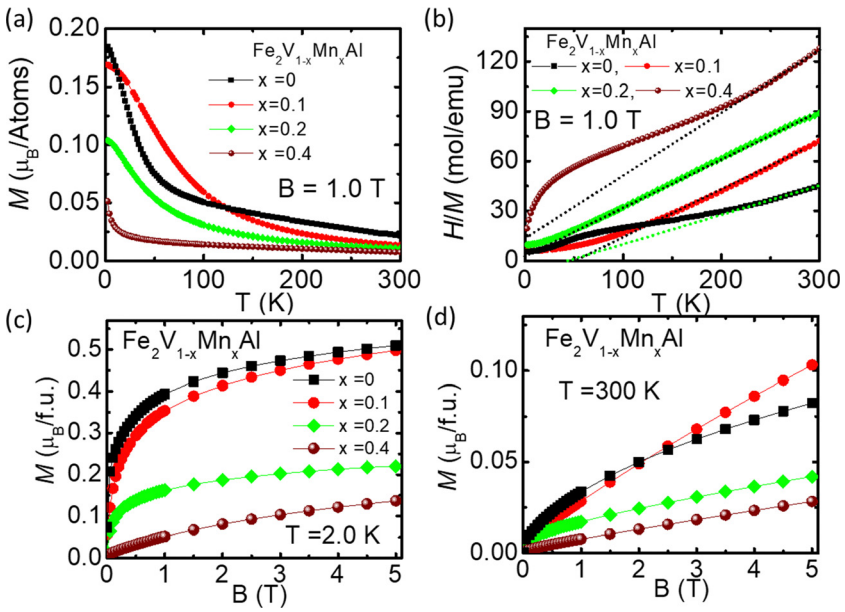

Fig. 8 (a) The temperature dependence of magnetization M for $Fe_2V_{1-x}Mn_xAl$ (x = 0, 0.1, 0.2, 0.4), (b) The inverse of magnetic susceptibility H/M *vs.* T for $Fe_2V_{1-x}Mn_xAl$ (x = 0, 0.1, 0.2, 0.4). The dotted line shows the fitting to the Curie–Weiss function $H/M = (T - \theta)/C$ with $C = NP_{eff}^2/3k_B$, where P_{eff}, N, and k_B are the effective magnetic moment, number of magnetic ions and the Boltzmann constant, respectively. (c) and (d) The magnetization M *vs.* B curves for $Fe_2V_{1-x}Mn_xAl$ (x = 0, 0.1, 0.2, 0.4) at 2.0 K and 300 K.

Table 1 Obtained results from Curie–Weiss function $H/M = (T - \theta)/C$ for the $Fe_2V_{1-x}Mn_xAl$ samples

Samples	C (K emu mol^{-1})	μ_{eff} (μ_B per atoms)	θ (K)
$x = 0$	5.88	3.44	35
$x = 0.1$	4.05	2.87	50
$x = 0.2$	3.59	2.69	−2.5
$x = 0.4$	2.46	1.85	−14.6

expected due to the antiferromagnetic correlation between Mn atoms. The higher Mn concentration, for example, the $x \geq 0.2$ samples, probably shows a ferrimagnetic nature, which is analogous to the ferrimagnetism reported in the Fe_2MnAl compound.[82] However, above the Curie point, the inverse magnetic susceptibility is no longer following the Néel hyperbola. This deviation is due to the limitations of magnetization measurements in the paramagnetic state of the alloys without perfect atomic ordering. The effective magnetic moments evaluated from the respective Curie constants C are $\mu_{eff} = 3.44\mu_B$ per atoms for $x = 0$, $\mu_{eff} = 2.87\mu_B$ per atoms for $x = 0.1$, $\mu_{eff} = 2.69\mu_B$ per atoms for $x = 0.2$, and $\mu_{eff} = 1.85\mu_B$ per atoms for $x = 0.4$. The μ_{eff} values for $x \leq 0.2$ are close to those calculated for $Fe_2V_{0.9}Cr_{0.1}Al$ and other Fe_2VAl-based full-Heusler compounds *etc.*[31,53,83]

Beyond that, it is interesting to point out that the Seebeck coefficient of the Mn-doped $Fe_2V_{1-x}Mn_xAl$ exhibits its maximum value of about 60 μV K^{-1} at 300 K for a wide range of Mn concentrations, $x = 0.1$ to 0.4, as seen in Fig. 2(b). This plateau-like behavior cannot be explained by a normal doping dependence (see Fig. 6(a)). In addition, the magnetic interaction is also found to be reduced by Mn-doping, as is seen in Fig. 8. The undoped Fe_2VAl shows large effective magnetic moment $\mu_{eff} = 3.44\mu_B$ per atoms, which suggests off-stoichiometry or Fe antisite defects is present in the sample. The values of effective magnetic moments decrease with increasing Mn doping levels in $Fe_2V_{1-x}Mn_xAl$. We can assume that at low Mn doping level, isolated magnetic ions might act as local perturbations, but their influence on the overall magnetic interaction might be minimal. As the Mn doping level increases, the competing interactions could become more pronounced, potentially leading to a more significant reduction in magnetic interaction. Consequently, the Mn-doped samples need to assume other changes in the electronic structure emerging from the substitution of Mn atoms at the V sublattice that cause an enhancement of the Seebeck coefficient.

The magnetization (M) as a function of applied magnetic field (B) for $Fe_2V_{1-x}Mn_xAl$ ($x = 0.1$, 0.2, 0.4) is shown in Fig. 8(c) and (d) at 2.0 K and 300 K, respectively. The magnetization curves up to $B = 5$ T reveal a gradual change, from ferromagnetic-like features ($x = 0.1$) towards a paramagnetic behaviour for $x = 0.4$. Most importantly, the magnetization decreases with increasing Mn concentration. It might be possible that introducing Mn magnetic ions at the V site in Fe_2VAl could create several competing magnetic interactions. Depending on the specific magnetic ion and its interactions with Fe and Al, these competing interactions might partially cancel out the ferromagnetic order between Fe atoms, leading to a net reduction in the overall magnetic interaction strength. Also, we have studied magnetic properties for Al-rich $Fe_2V_{0.9}Mn_{0.1}Al_{1+y}$ compounds [see ESI,† Fig. S5(a)–(d)].

Density functional theory calculations

To further elucidate the anomalous behavior of Mn substitution in $Fe_2V_{1-x}Mn_xAl$, both with respect to the thermoelectric transport and magnetic properties, we performed extensive density functional theory (DFT) calculations on substituted $Fe_2V_{1-x}Mn_xAl$ Heusler compounds across different concentrations x. Our calculations indicate that Mn atoms, when substituted at the V site, exhibit a large local magnetic moment of around $2.43\mu_B$, while they stay non-magnetic, when substituted at the Fe sites.

To simulate the true paramagnetic state with thermally disordered magnetic moments at high temperatures, calculations were performed within the framework of the disordered

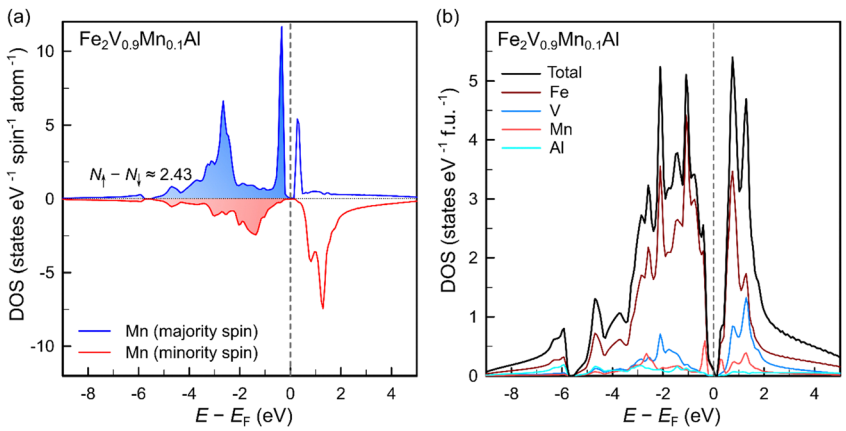

Fig. 9 (a) Spin-polarized density of states of a single Mn atom in $Fe_2V_{0.9}Mn_{0.1}Al$, showing a sizeable splitting between majority and minority contributions, yielding a large magnetic moment $m \sim 2.43\mu_B$ for Mn atoms substituted at the V site. (b) Partial atom-projected density of states of $Fe_2V_{0.9}Mn_{0.1}Al$.

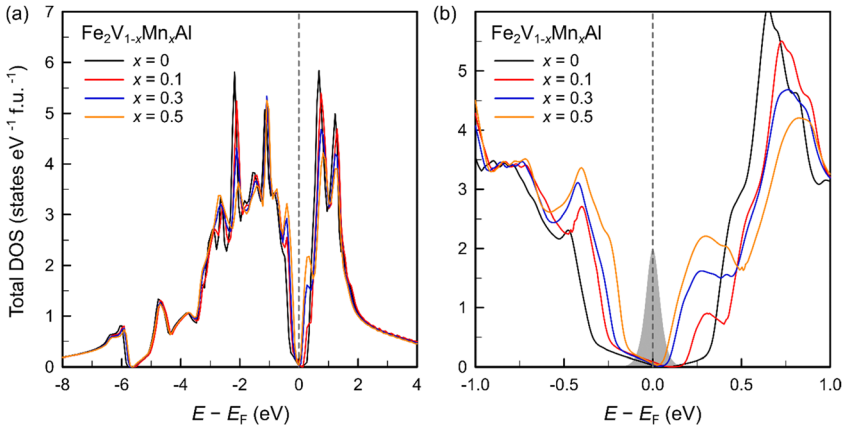

Fig. 10 (a) Total density of states (DOS) of $Fe_2V_{1-x}Mn_xAl$ calculated in the disordered local moment (DLM) theory. (b) DOS around the Fermi energy, featuring contributions from rather localized Mn impurity states at the valence and conduction band edges, as well as a pinning of the Fermi level within the pseudogap. To indicate the energy range, relevant for thermoelectric transport, the derivative of the Fermi–Dirac distribution at 300 K is shown in grey.

local moment (DLM) approximation.[67] Moreover, the substitutional alloy disorder due to Mn atoms randomly replacing V atoms in the unit cell, is fully accounted for in the calculations of the electronic structure by making use of the Coherent Potential Approximation (CPA).[63] Fig. 9(a) shows the atom-projected and spin-polarized density of states of a single Mn atom in $Fe_2V_{0.9}Mn_{0.1}Al$. A sizeable splitting between majority and minority spin channels is obvious, resulting in a large magnetic moment of around $2.43\mu_B$. Interestingly, both minority- and majority-spin contributions exhibit a gap at the Fermi energy. Moreover, rather sharp and localized features in the electronic density of states occur at both sides of the Fermi level for the majority-spin bands. These impurity states contribute to the total DOS of $Fe_2V_{1-x}Mn_xAl$ at the conduction and valence band edge as shown in Fig. 10(b), effectively narrowing the pseudogap of pristine Fe_2VAl with increasing Mn substitution.

Fig. 9(b) displays the atom-projected partial DOS of $Fe_2V_{0.9}Mn_{0.1}Al$ in the paramagnetic state with the respective contributions from all atoms. We point out that, despite the large electron doping concentration of 0.2 e per formula unit upon substituting 10% Mn at the V site, the Fermi level remains virtually unaffected and stays within the pseudogap. This becomes even more evident in Fig. 10, where the total DOS of $Fe_2V_{1-x}Mn_xAl$ is shown for various Mn concentrations in the paramagnetic state, matching our experimentally investigated samples. Even for Mn substitutions as high as $x = 0.5$, corresponding to an entire additional electron, the Fermi level remains pinned within the pseudogap and does not get shifted into the conduction band. The anomalous doping behavior can be traced back to Mn forming magnetic impurity states below the Fermi energy (see Fig. 10(a)), which can accommodate the additional electrons doped by Mn in $Fe_2V_{1-x}Mn_xAl$. Thus, although the valence electron concentration increases, the total number of states below E_F increases as well, rendering an unchanged position of E_F. This readily explains the unconventional VEC dependence of the Seebeck coefficient in Fig. 7(a), where S retains positive values even for VEC $\gg$ 6.

We also studied the effect of substituting Mn at the Fe site, *i.e.*, considering that Mn may occupy the Fe site with Fe atoms simultaneously occupying the vacant V positions as antisite defects ($Fe_{1.9}Mn_{0.1}V_{0.9}Fe_{0.1}Al$), which cannot be ruled out by our standard X-ray diffraction experiments due to the very similar atomic scattering factors of Mn, Fe and V. However, the electronic density of states of $Fe_{1.9}Mn_{0.1}V_{0.9}Fe_{0.1}Al$ (see ESI,† Fig. S8) indicates that this seems very unlikely, since a metallic ground state with a very large DOS at E_F emerges, which contradicts the experimental Seebeck coefficient and its VEC dependence.

Conclusion

Overall, p-type Fe_2VAl compounds are less developed compared to n-type ones. Here, we performed a systematic experimental and theoretical study of the thermoelectric properties of Mn-doped $Fe_2V_{1-x}Mn_xAl$ Heusler compounds across a wide range of Mn concentrations x = 0 – 0.6. We found an unexpected hole-dominated Seebeck coefficient in nominally n-doped $Fe_2V_{1-x}Mn_xAl$. Using DFT calculations, the origin for this unconventional doping behavior was found to be rooted in distinct modifications of the electronic density of states upon Mn substitution. More specifically, Mn atoms at the V site form magnetic impurity states with a large local magnetic moment ($m \sim 2.43\mu_B$) and antiferromagnetic exchange interactions. The additional electronic states contributed below E_F exactly balance the chemical potential, such that E_F remains pinned at the valence band edge, within the pseudogap, even for very large Mn concentrations up to $x = 0.6$. Moreover, rather localized Mn states spawn at both sides of the pseudogap, yielding an increase of the DOS effective mass, albeit a narrowing of the pseudogap is triggered as well. Consequently, relatively large p-type Seebeck coefficients and an anomalous doping/VEC dependence emerges in $Fe_2V_{1-x}Mn_xAl$.

The thermoelectric properties could be further improved by co-substituting Al antisites at the Fe and V sublattices in

Al-rich $Fe_2V_{0.9}Mn_{0.1}Al_{1+y}$ compounds. $Fe_2V_{0.9}Mn_{0.1}Al_{1.1}$ exhibits the largest Seebeck coefficient (S = 75 μV K^{-1}) and PF = 2.2 mW K^{-2} m^{-1} at T = 350 K. Also, the thermal conductivity decreased to 9 W m^{-1} K^{-1} for $Fe_2V_{0.9}Mn_{0.1}Al_{1.5}$ (y = 0.5). Consequently, the largest ZT value, ∼0.1, was found for $Fe_2V_{0.9}Mn_{0.1}Al_{1.5}$ (y = 0.5), at T = 500 K. Our study motivates further investigations and optimization studies of Fe_2VAl-based Heusler compounds, co-substituted with Mn at the V site, to realize high-performance p-type thermoelectrics, which are relevant for technological applications.

Conflicts of interest

There are no conflicts to declare.

Acknowledgements

This work was mainly supported by JST Mirai Program Grant JPMJMI19A1. N. T. has been supported by JSPS KAKENHI, 22H01761.

References

1 L. E. Bell, *Science*, 2008, **321**, 1457.
2 J. Heand and T. M. Tritt, *Science*, 2017, **357**, eaak9997.
3 N. Nandihalli, C.-J. Liu and T. Mori, *Nano Energy*, 2020, **78**, 105186.
4 I. Petsagkourakis, K. Tybrandt, X. Crispin, I. Ohkubo, N. Satoh and T. Mori, *Sci. Technol. Adv. Mater.*, 2018, **19**, 836.
5 T. Zhu, Y. Liu, C. Fu, J. P. Heremans, J. G. Snyder and X. Zhao, *Adv. Mater.*, 2017, **29**, 1605884.
6 Z. Liu, N. Sato, W. Gao, K. Yubuta, N. Kawamoto, M. Mitome, K. Kurashima, Y. Owada, K. Nagase, C.-H. Lee, J. Yi, K. Tsuchiya and T. Mori, *Joule*, 2021, **5**, 1196.
7 T. Mori, *Small*, 2017, **13**, 1702013.
8 J. Mao, Z. Liu, J. Zhou, H. Zhu, Q. Zhang, G. Chen and Z. Ren, *Adv. Phys.*, 2018, **67**, 69–147.
9 T. Hendricks, T. Caillat and T. Mori, *Energies*, 2022, **15**, 7307.
10 Y. Nishino, M. Kato, S. Asano, K. Soda, M. Hayasaki and U. Mizutani, *Phys. Rev. Lett.*, 1997, **79**, 1909.
11 H. Kato, M. Kato, Y. Nishino, U. Mizutani and S. Asano, *J. Jpn. Inst. Met.*, 2001, **65**, 652.
12 Y. Nishino and Y. Tamada, *J. Appl. Phys.*, 2014, **115**, 123707.
13 G. Y. Guo, G. A. Botton and Y. Nishino, *J. Phys.: Condens. Matter*, 1998, **10**, L119.
14 D. J. Singh and I. I. Mazin, *Phys. Rev. B: Condens. Matter Mater. Phys.*, 1998, **57**, 14352.
15 R. Weht and W. E. Pickett, *Phys. Rev. B: Condens. Matter Mater. Phys.*, 1998, **58**, 6855.
16 A. Laila, M. Nanko and M. Takeda, *Mater. Trans.*, 2020, **61**, 2216.
17 M. Weinert and R. E. Watson, *Phys. Rev. B: Condens. Matter Mater. Phys.*, 1998, **58**, 9732.
18 H. Okamura, J. Kawahara, T. Nanba, S. Kimura, K. Soda, U. Mizutani, Y. Nishino, M. Kato, I. Shimoyama, H. Miura, K. Fukui, K. Nakagawa, H. Nakagawa and T. Kinoshita, *Phys. Rev. Lett.*, 2000, **84**, 3674.
19 F. Garmroudi, A. Riss, M. Parzer, N. Reumann, H. Muller, E. Bauer, S. Khmelevskyi, R. Podloucky, T. Mori, K. Tobita, Y. Katsura and K. Kimura, *Phys. Rev. B*, 2021, **103**, 085202.
20 F. Garmroudi, M. Parzer, A. Riss, A. V. Ruban, S. Khmelevskyi, M. Reticcioli, M. Knopf, H. Michor, A. Pustogow, T. Mori and E. Bauer, *Nat. Commun.*, 2022, **13**, 3599.
21 F. Garmroudi, M. Parzer, A. Riss, N. Reumann, B. Hinterleitner, K. Tobita, Y. Katsura, K. Kimura, T. Mori and E. Bauer, *Acta Mater.*, 2021, **212**, 116867.
22 F. Garmroudi, M. Parzer, A. Riss, S. Beyer, S. Khmelevskyi, T. Mori, M. Reticcioli and E. Bauer, Materials Today, *Physics*, 2022, **27**, 100742.
23 Z. Liu, W. Gao, H. Oshima, K. Nagase, C.-H. Lee and T. Mori, *Nat. Commun.*, 2022, **13**, 1120.
24 K. Imasato, S. D. Kang and G. J. Snyder, *Energy Environ. Sci.*, 2019, **12**, 965–971.
25 L. Wang, N. Sato, Y. Peng, R. Chetty, N. Kawamoto, D. H. Nguyen and T. Mori, Advanced Energy, *Materials*, 2023, **13**, 2301667.
26 Y. C. Lan, B. Poudel, Y. Ma, D. Z. Wang, M. S. Dresselhaus, G. Chen and Z. F. Ren, *Nano Lett.*, 2009, **9**, 1419.
27 Y.-Z. Li, Q. Zhang, K. Liu, Y.-J. Lin, N. Lin, Y. Yu, F. Liu, X.-B. Zhao, B.-H. Ge, O. Cojocaru-Mirédin, C.-G. Fu and T.-J. Zhu, Materials Today, *NANO*, 2023, **22**, 100340.
28 J. Pei, B. Cai, H.-L. Zhuang and J.-F. Li, *Natl. Sci. Rev.*, 2020, **7**, 1856–1858.
29 Y. Feng, J. Y. Rhee, T. A. Wiener, D. W. Lynch, B. E. Hubbard, A. J. Sievers, D. L. Schlagel, T. A. Lograsso and L. L. Miller, *Phys. Rev. B: Condens. Matter Mater. Phys.*, 2001, **63**, 165109.
30 K. Soda, H. Murayama, K. Shimba, S. Yagi, J. Yuhara, T. Takeuchi, U. Mizutani, H. Sumi, M. Kato, H. Kato, Y. Nishino, A. Sekiyama, S. Suga, T. Matsushita and Y. Saito, *Phys. Rev. B: Condens. Matter Mater. Phys.*, 2005, **71**, 245112.
31 M. Kato, Y. Nishino, U. Mizutani and S. Asano, *J. Phys.: Condens. Matter*, 2000, **12**, 1769–1779.
32 T. Naka, K. Sato, M. Taguchi, T. Nakane, F. Ishikawa, Y. Yamada, Y. Takaesu, T. Nakama and A. Matsushita, *Phys. Rev. B: Condens. Matter Mater. Phys.*, 2012, **85**, 085130.
33 S. Jemima, A. Mani, A. Bharathi, N. Ravindran and Y. Hariharan, *J. Alloys Compd.*, 2001, **326**, 183–187.
34 E. P. Amaladass, A. T. Satya, S. Sharma, K. Vinod, V. Srinivas, C. S. Sundar and A. Bharathi, *J. Alloys Compd.*, 2015, **648**, e34–e38.
35 O. Nashima, T. Kanomata, Y. Yamaguchi, S. Abe, T. Harada, T. Suzuki, H. Nishihara, K. Koyama, T. Shishido, K. Watanabe and T. Kaneko, *J. Alloys Compd.*, 2004, **383**, 298–301.
36 M. Mikami, Y. Kinemuchi, K. Ozaki, Y. Terazawa and T. Takeuchi, *J. Appl. Phys.*, 2012, **111**, 093710.

37 R. Jha, N. Tsujii, C. Bourgès, W. Gao, E. Bauer and T. Mori, *Z. Anorg. Allg. Chem.*, 2022, **648**, e202200058.
38 W. Lu, W. Zhang and L. Chen, *J. Alloys Compd.*, 2009, **484**, 812–815.
39 F. Kobayashi, N. Ide and Y. Nishino, *J. Jpn. Inst. Met.*, 2007, **71**, 208.
40 Y. Nishino, *IOP Conf. Ser.: Mater. Sci. Eng.*, 2011, **18**, 142001.
41 T. Sugiura and Y. Nishino, *J. Jpn. Inst. Met.*, 2009, **73**, 846.
42 Y. Sandaiji, N. Ide, Y. Nishino, T. Owada, S. Harada and K. Soda, *J. Jpn. Soc. Powder Powder Metall.*, 2010, **57**, 207.
43 I. Knapp, B. Budinska, D. Milosavljevic, P. Heinrich, S. Khmelevskyi, R. Moser, R. Podloucky, P. Prenninger and E. Bauer, *Phys. Rev. B*, 2017, **96**, 045204.
44 K. Iwase, Y. Nishino, H. Miyazaki and K. Soda, *J. Jpn. Inst. Met.*, 2008, **72**, 464.
45 Y. Nishino, H. Kato, M. Kato and U. Mizutani, *Phys. Rev. B: Condens. Matter Mater. Phys.*, 2001, **63**, 233303.
46 Y. Hanada, R. O. Suzuki and K. Ono, *J. Alloys Compd.*, 2001, **329**, 63.
47 C. S. Lue and Y.-K. Kuo, *Phys. Rev. B: Condens. Matter Mater. Phys.*, 2002, **66**, 085121.
48 T. Nakama, Y. Takaesu, K. Yagasaki, T. Naka, A. Matsushita, K. Fukuda and Y. Yamada, *J. Phys. Soc. Jpn.*, 2005, **74**, 1378.
49 Y. Nishino, S. Kamizono, H. Miyazaki and K. Kimura, *AIP Adv.*, 2019, **9**, 125003.
50 B. Hinterleitner, I. Knapp, M. Poneder, Y. Shi, H. Müller, G. Eguchi, C. Eisenmenger-Sittner, M. Stöger-Pollach, Y. Kakefuda, N. Kawamoto, Q. Guo, T. Baba, T. Mori, S. Ullah, X.-Q. Chen and E. Bauer, *Nature*, 2019, **576**, 85–90.
51 H. Matsuura, Y. Nishino, U. Mizutani and S. Asano, *J. Jpn. Inst. Met.*, 2002, **66**, 767.
52 H. Miyazaki, S. Tanaka, N. Ide, K. Soda and Y. Nishino, *Mater. Res. Express*, 2014, **1**, 015901.
53 N. Tsujii, A. Nishide, J. Hayakawa and T. Mori, *Sci. Adv.*, 2019, **5**, eaat5935.
54 R. Ang, A. U. Khan, N. Tsujii, K. Takai, R. Nakamura and T. Mori, *Angew. Chem., Int. Ed.*, 2015, **54**, 12909.
55 F. Ahmed, N. Tsujii and T. Mori, *J. Mater. Chem. A*, 2017, **5**, 7545.
56 Y. Zheng, T. Lu, Md. M. H. Polash, M. Rasoulianboroujeni, N. Liu, M. E. Manley, Y. Deng, P. J. Sun, X. L. Chen, R. P. Hermann, D. Vashaee, J. P. Heremans and H. Zhao, *Sci. Adv.*, 2019, **5**, eaat9461.
57 J.-B. Vaney, S. Aminorroaya Yamini, H. Takaki, K. Kobayashi, N. Kobayashi and T. Mori, *Mater. Today Phys.*, 2019, **9**, 100090.
58 S. Hebert, R. Daou, A. Maignan, S. Das, A. Banerjee, C. Bourgès, N. Tsujii and T. Mori, *Sci. Technol. Adv. Mater.*, 2021, **22**, 583.
59 W. L. Lee, S. Watauchi, V. L. Miller, R. J. Cava and N. P. Ong, *Phys. Rev. Lett.*, 2004, **93**, 226601.
60 R. Ramos, M. H. Aguirre, A. Anadon, J. Blasco, I. Lucas, K. Uchida, P. A. Algarabel, L. Morellón, E. Saitoh and M. R. Ibarra, *Phys. Rev. B: Condens. Matter Mater. Phys.*, 2014, **90**, 054422.
61 H. Matsuura, M. Ogata, T. Mori and E. Bauer, *Phys. Rev. B*, 2021, **104**, 214421.
62 J. P. Perdew, K. Burke and M. Ernzerhof, *Phys. Rev. Lett.*, 1996, **77**, 3865.
63 B. L. Gyorffy, *Phys. Rev. B: Solid State*, 1972, **5**, 2382.
64 F. Izumi and K. Momma, *Solid State Phenom.*, 2007, **130**, 15.
65 I. A. Abrikosov and H. L. Skriver, *Phys. Rev. B: Condens. Matter Mater. Phys.*, 1993, **47**, 16532.
66 A. V. Ruban and H. L. Skriver, *Comput. Mater. Sci.*, 1999, **15**, 199.
67 B. L. Gyorffy, A. J. Pindor, J. Staunton, G. M. Stocks and H. Winter, *J. Phys. F: Met. Phys.*, 1985, **15**, 1337.
68 A. Denton and N. Ashcroft, *Phys. Rev. A: At., Mol., Opt. Phys.*, 1991, **43**, 3161.
69 M. Parzer, F. Garmroudi, A. Riss, S. Khmelevskyi, T. Mori and E. Bauer, *Appl. Phys. Lett.*, 2022, **120**, 071901.
70 F. Garmroudi, M. Parzer, A. Riss, A. Pustogow, T. Mori and E. Bauer, *Phys. Rev. B*, 2023, **107**, L081108.
71 B. Hinterleitner, F. Garmroudi, N. Reumann, T. Mori, E. Bauer and R. Podloucky, *J. Mater. Chem. C*, 2021, **9**, 2073–2085.
72 K. Kurosaki, H. Muta, Y. Endo, A. Charoenphakdee, M. Uno and S. Yamanaka, *J. Alloys Compd.*, 2009, **486**, 507–510.
73 Y. Takagiwa and Y. Iwasaki, *ACS Appl. Energy Mater.*, 2023, **6**(15), 8256–8265.
74 Y. Nishino, S. Deguchi and U. Mizutani, *Phys. Rev. B: Condens. Matter Mater. Phys.*, 2006, **74**, 115115.
75 B. Hinterleitner, P. Fuchs, J. Rehak, F. Garmroudi, M. Parzer, M. Waas, R. Svagera, S. Steiner, M. Kishimoto, R. Moser, R. Podloucky and E. Bauer, *Phys. Rev. B*, 2020, **102**, 075117.
76 Y. Nishino, H. Sumi and U. Mizutani, *Phys. Rev. B: Condens. Matter Mater. Phys.*, 2005, **71**, 094425.
77 C. S. Lue, C. F. Chen and K. Kuo, *Phys. Rev. B: Condens. Matter Mater. Phys.*, 2007, **75**, 064204.
78 M. Mikami and K. Kobayashi, *J. Alloys Compd.*, 2008, **466**, 530–534.
79 K. Soda, S. Harada, M. Kato, S. Yagi, M. Inukai, H. Miyazaki, Y. Sandaiji, Y. Tamada, S. Tanaka, T. Sugiura and Y. Nishino, *J. Electron Spectrosc. Relat. Phenom.*, 2011, **184**, 236.
80 K. Soda, S. Harada, M. Kato, S. Yagi, Y. Sandaiji and Y. Nishino, *IOP Conf. Ser.: Mater. Sci. Eng.*, 2011, **18**, 142004.
81 G. J. Snyder, A. Pereyra and R. Gurunathan, *Adv. Funct. Mater.*, 2022, **32**, 2112772.
82 N. I. Kourov, V. V. Marchenkov, A. V. Korolev, L. A. Stashkova, S. M. Emelyanova and H. W. Weber, *Phys. Solid State*, 2015, **57**, 700–708.
83 K. Sato, T. Naka, M. Taguchi, T. Nakane, F. Ishikawa, Y. Yamada, Y. Takaesu, T. Nakama, A. de Visser and A. Matsushita, *Phys. Rev. B: Condens. Matter Mater. Phys.*, 2010, **82**, 104408.

